

# Assembling 2D MXenes into Highly Stable Pseudocapacitive Electrodes with High Power and Energy Densities

Armin Vahid Mohammadi, Mehrnaz Mojtabavi, Nuala Mai Caffrey, Meni Wanunu, and Majid Beidaghi\*

Electrochemical capacitors (ECs) that store charge based on the pseudocapacitive mechanism combine high energy densities with high power densities and rate capabilities. 2D transition metal carbides (MXenes) have been recently introduced as high-rate pseudocapacitive materials with ultrahigh areal and volumetric capacitances. So far, 20 different MXene compositions have been synthesized and many more are theoretically predicted. However, since most MXenes are chemically unstable in their 2D forms, to date only one MXene composition,  $\text{Ti}_3\text{C}_2\text{T}_x$ , has shown stable pseudocapacitive charge storage. Here, a cation-driven assembly process is demonstrated to fabricate highly stable and flexible multilayered films of  $\text{V}_2\text{CT}_x$  and  $\text{Ti}_2\text{CT}_x$  MXenes from their chemically unstable delaminated single-layer flakes. The electrochemical performance of electrodes fabricated using assembled  $\text{V}_2\text{CT}_x$  flakes surpasses  $\text{Ti}_3\text{C}_2\text{T}_x$  in various aqueous electrolytes. These electrodes show specific capacitances as high as  $1315 \text{ F cm}^{-3}$  and retain  $\approx 77\%$  of their initial capacitance after one million charge/discharge cycles, an unprecedented performance for pseudocapacitive materials. This work opens a new venue for future development of high-performance supercapacitor electrodes using a variety of 2D materials as building blocks.

Fast storage and delivery of electrical energy for powering mobile electronics and electric vehicles is an evolving challenge in the field of energy storage. Despite considerable progress in the design and fabrication of the state-of-the-art batteries,

A. Vahid Mohammadi, Prof. M. Beidaghi  
Department of Mechanical and Materials Engineering  
Auburn University  
Auburn, AL 36849, USA  
E-mail: mbeidaghi@auburn.edu

M. Mojtabavi, Prof. M. Wanunu  
Department of Bioengineering  
Northeastern University  
Boston, MA 02115, USA

Dr. N. M. Caffrey  
School of Physics and CRANN  
Trinity College  
Dublin 2, Ireland

Prof. M. Wanunu  
Department of Physics  
Northeastern University  
Boston, MA 02115, USA

 The ORCID identification number(s) for the author(s) of this article can be found under <https://doi.org/10.1002/adma.201806931>.

DOI: 10.1002/adma.201806931

their charging rates and lifespans have remained insufficient for many applications.<sup>[1,2]</sup> In contrast, electrochemical capacitors (ECs), also known as supercapacitors, can be charged and discharged in seconds and deliver high power densities for thousands of cycles.<sup>[2–6]</sup> However, in conventional ECs or electric double-layer capacitors (EDLCs), charge storage is based on the electrosorption of ions on the surface of carbonaceous electrode materials and, therefore, the amount of stored charge is limited by the surface area of the electrodes. Pseudocapacitive materials, an alternative subclass of ECs, can store more charge and deliver higher energy densities as compared to EDLCs through a storage mechanism that involves fast and reversible surface redox reactions.<sup>[1,2,5,7–10]</sup> For most materials in this category (e.g., metal oxides such as  $\text{RuO}_2 \cdot n\text{H}_2\text{O}$ ,<sup>[9]</sup> and  $\text{MnO}_2$ ,<sup>[2]</sup>), the redox reactions are limited to the surface or near-surface of the electrodes, which greatly underutilizes the

bulk of electrode material in charge storage. For some oxides such as  $\text{T-Nb}_2\text{O}_5$ ,<sup>[11]</sup> the pseudocapacitance occurs in the bulk of the material through fast intercalation of ions resulting in high specific capacitances and energy densities. However, transition metal oxides suffer from low electrical conductivities which hinders their rate-handling capability, power density, and cyclic performance.<sup>[3,5,12]</sup>

2D transition metal carbides and nitrides (MXenes) are a class of 2D materials with promising properties for energy storage applications.<sup>[3,5,12,13]</sup> These materials have a general formula of  $\text{M}_{n+1}\text{X}_n\text{T}_x$ , where M is a transition metal, X is carbon and/or nitrogen,  $n$  can be 1, 2, or 3, and  $\text{T}_x$  represents surface functional groups.<sup>[14–16]</sup> MXenes exhibit high electrical conductivities, can be intercalated with various organic and inorganic ions, and can undergo fast redox reactions at their surfaces.<sup>[17]</sup> Such properties are ideal for pseudocapacitive charge storage. Intercalation-based pseudocapacitive charge storage in MXenes was first reported for delaminated  $\text{Ti}_3\text{C}_2\text{T}_x$  (d- $\text{Ti}_3\text{C}_2\text{T}_x$ ), where freestanding film electrodes showed volumetric capacitances of over  $400 \text{ F cm}^{-3}$  in aqueous electrolytes.<sup>[5]</sup> In addition, volumetric capacitances as high as  $\approx 900 \text{ F cm}^{-3}$  have been reported for freestanding d- $\text{Ti}_3\text{C}_2\text{T}_x$  films in sulfuric acid electrolytes.<sup>[13]</sup> Recently, Lukatskaya et al.<sup>[3]</sup> demonstrated that some electrochemical properties of MXene electrodes, such as their

specific capacitance and rate-handling capability, can be further improved by designing microporous and hydrogel electrode structures. However, of the 20 different MXenes that have been synthesized so far, only  $\text{Ti}_3\text{C}_2\text{T}_x$  has been systematically investigated as a pseudocapacitive electrode material for ECs, mainly due to the low chemical or electrochemical stability of 2D flakes of other MXene compositions. Notably, the pseudocapacitive properties of completely delaminated (single/few layers)  $\text{M}_2\text{CT}_x$  MXenes, such as  $\text{d-V}_2\text{CT}_x$  and  $\text{d-Ti}_2\text{CT}_x$ , have remained unexplored. When these MXenes are delaminated to single/few-layer sheets they show poor chemical stability in ambient conditions, or in the presence of water and oxygen.<sup>[17,18]</sup> For example, multilayered  $\text{V}_2\text{CT}_x$ , which has shown the highest Li ion intercalation capacity among all MXenes,<sup>[19,20]</sup> quickly oxidizes in water or air when delaminated to 2D flakes ( $\text{d-V}_2\text{CT}_x$ ). Very recently, Shan et al. showed the promise of  $\text{V}_2\text{CT}_x$  MXene as aqueous supercapacitor electrode in a short report.<sup>[21]</sup> However, despite a promising electrochemical performance, the  $\text{V}_2\text{CT}_x$  showed low electrochemical stability, which was attributed to either oxidation of MXene or dissolution of V in aqueous electrolytes.<sup>[21]</sup> To date, the low chemical and electrochemical stability of  $\text{V}_2\text{CT}_x$  and other  $\text{M}_2\text{C}$  MXenes has prevented the systematic study of their pseudocapacitive properties.

Here, we demonstrate highly stable, freestanding, and flexible pseudocapacitive electrodes fabricated by the cation-driven assembly of otherwise unstable  $\text{V}_2\text{CT}_x$  flakes. The assembled flakes have a layered structure that can be intercalated by a variety of inorganic cations and can deliver outstanding high-rate electrochemical performances with volumetric capacitances in excess of  $1300 \text{ F cm}^{-3}$ . The fabricated  $\text{V}_2\text{CT}_x$  films exhibit superior stability in ambient atmospheres and aqueous electrolytes with capacitance retention of  $\approx 77\%$  after one million charge/discharge cycles, an unprecedented performance for MXene electrodes. In addition, symmetric cells fabricated with assembled  $\text{V}_2\text{CT}_x$  electrodes delivered high volumetric energy and power densities of  $0.203 \text{ Wh cm}^{-3}$  and  $28.15 \text{ W cm}^{-3}$ , respectively, which are among the highest values reported for supercapacitors to date.

$\text{V}_2\text{CT}_x$  is expected to be an excellent pseudocapacitive material as the multiple oxidation states of V can potentially lead to a high charge storage capacitance.<sup>[20,22]</sup> We synthesized  $\text{d-V}_2\text{CT}_x$  flakes by delaminating multilayered  $\text{V}_2\text{CT}_x$  (ML- $\text{V}_2\text{CT}_x$ ) particles, which were in turn synthesized by selectively etching Al atoms from a  $\text{V}_2\text{AlC}$  MAX phase powder (details of the experimental methods are available in the Supporting Information). The final product of the synthesis process (described in more detail in the Supporting Information) is a dispersion of  $\text{d-V}_2\text{CT}_x$  flakes in water. As shown in **Figure 1a**, when the dispersion is kept in ambient atmosphere,  $\text{d-V}_2\text{CT}_x$  flakes quickly oxidize and disintegrate within a few hours, as evidenced by a change in color of the dispersion from dark green to pale yellow. Deaeration of the produced dispersion and storage in a sealed container slows the degradation of  $\text{d-V}_2\text{CT}_x$  flakes. However, atomic force microscopy (AFM) images (**Figure 1b,c** and **Figure S3**, Supporting Information) suggested that even the flakes stored in deaerated containers oxidize and disintegrate in about two days. In addition, freestanding MXene films fabricated by vacuum filtration of fresh  $\text{d-V}_2\text{CT}_x$  dispersions showed little flexibility and their color changed from grayish brown to black

after one week of exposure to ambient atmosphere at room temperature (**Figure 1d**). The fabricated films disintegrated, and their color further darkened after one month.

The X-ray photoelectron spectroscopy (XPS) spectrum (V 2p region) of a freshly prepared  $\text{d-V}_2\text{CT}_x$  film (**Figure 1e**) showed that vanadium is mostly present in its  $\text{V}^{4+}$  oxidation state, indicating the termination of MXene surface with functional groups and presence of surface oxide monolayers, in agreement with previous studies (see Table S1 in the Supporting Information for XPS peak positions and ratios).<sup>[19,20]</sup> However, the XPS spectrum of a one-month-old film (**Figure 1f**) confirmed the oxidation of  $\text{V}_2\text{CT}_x$  flakes, as the V species were dominated by  $\text{V}^{5+}$ , indicating the formation of  $\text{V}_2\text{O}_5$ . Previous studies<sup>[23,24]</sup> have shown that the products of  $\text{Ti}_3\text{C}_2\text{T}_x$  MXene oxidation at room temperature are amorphous oxide particles and carbon. This also appears to be the case for  $\text{V}_2\text{CT}_x$  oxidation. The X-ray diffraction (XRD) pattern of the oxidized  $\text{d-V}_2\text{CT}_x$  films (**Figure 1g**) showed a significant loss of intensity for the (0002) MXene peak. However, no peaks related to vanadium oxide species were observed, implying that the produced vanadium oxide is amorphous in nature.

The self-restacking of the  $\text{d-V}_2\text{CT}_x$  flakes and their instability adversely affect the electrochemical performance of the fabricated freestanding MXene films. **Figure 1h,i** show cyclic voltammetry (CV) profiles and cycle life of a  $\text{d-V}_2\text{CT}_x$  film electrode in a  $5 \text{ m LiCl}$  aqueous electrolyte. This electrode showed good pseudocapacitive performance at low scan rates, but its capacitive behavior declined at scan rates above  $10 \text{ mV s}^{-1}$ , suggesting a high ion transport resistance between the restacked MXene flakes.<sup>[3,25]</sup> In addition, due to the gradual oxidation of the electrodes during cycling (**Figure S7**, Supporting Information), a significant drop in the electrode capacitance (to  $\approx 69\%$  of the initial capacitance) was observed in less than 1500 cycles. To date, the instability of  $\text{d-V}_2\text{CT}_x$  in air and water has hindered its applications, and studies of the electrochemical properties of  $\text{V}_2\text{CT}_x$  MXenes have been mostly limited to more stable multilayered particles or to nonaqueous electrolytes to avoid oxidation.<sup>[19,20,26]</sup> In the following, we describe an approach for assembling  $\text{d-V}_2\text{CT}_x$  flakes into highly stable electrodes with significantly improved pseudocapacitive performance.

The assembly of 2D transition metal oxides into layered structures mediated by alkali metal cations has been recently utilized to synthesize preintercalated oxide materials for energy storage applications.<sup>[27–30]</sup> This simple and rapid assembly method relies on the electrostatic attraction of negatively charged 2D oxide flakes to alkali cations, forming ordered layered structures with improved electrochemical performance.<sup>[27,28,31]</sup> In the case of MXenes, it was recently reported that addition of alkali hydroxide solutions to  $\text{d-Ti}_3\text{C}_2\text{T}_x$  dispersions results in flocculation of MXene flakes and formation of porous aggregates with crumpled morphologies.<sup>[32]</sup> However, here we demonstrate that electrostatic interaction of cations and  $\text{V}_2\text{CT}_x$  flakes can be utilized to fabricate highly ordered, freestanding, and flexible films. This cation-driven assembly not only significantly improves the electrochemical properties of  $\text{V}_2\text{CT}_x$ , but also converts the chemically (and electrochemically) unstable MXene flakes to highly stable films and electrodes.

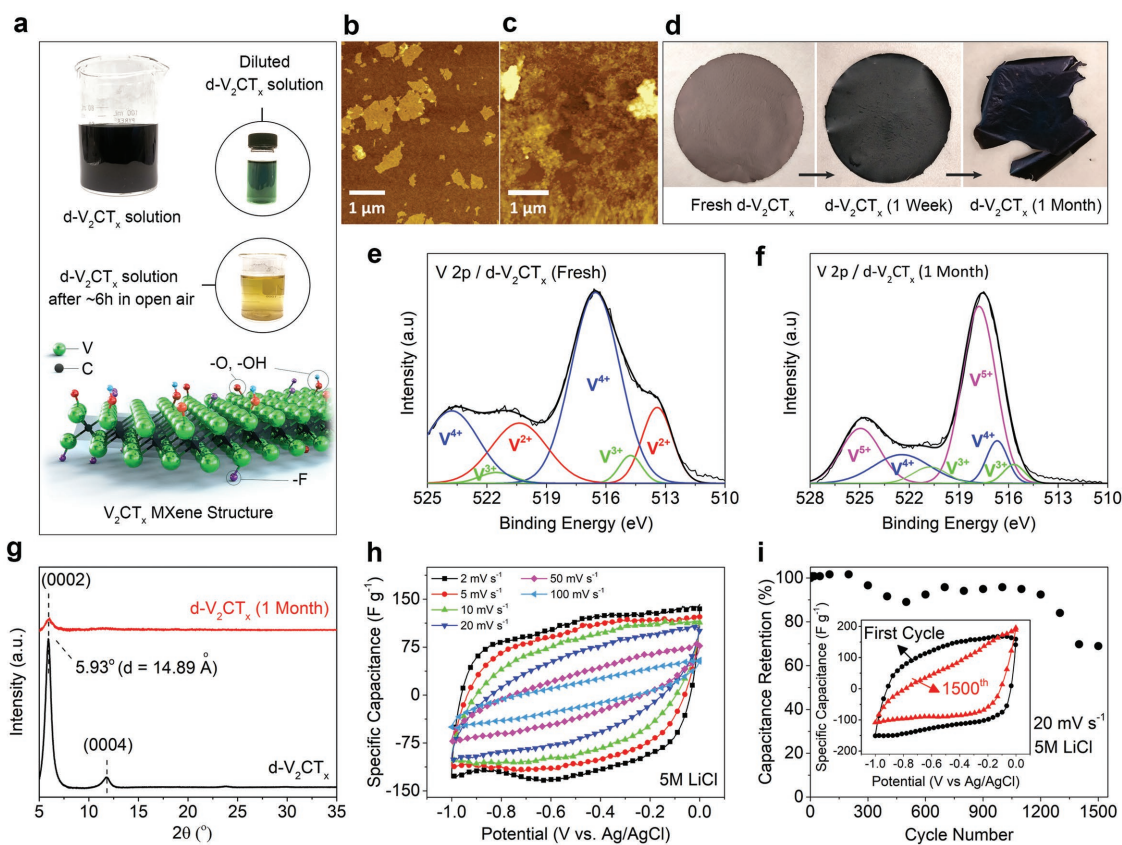


**Figure 1.** a) Digital photographs of a fresh  $d\text{-V}_2\text{CT}_x$  solution and a diluted  $d\text{-V}_2\text{CT}_x$  solution, showing an initial green color which changes to a pale yellow in few hours due to oxidation of the  $d\text{-V}_2\text{CT}_x$  flakes. Schematic of the structure of  $\text{V}_2\text{CT}_x$  MXene is shown at the bottom of this panel. b) An AFM image of a fresh single layer  $d\text{-V}_2\text{CT}_x$  MXene. c) An AFM image of  $d\text{-V}_2\text{CT}_x$  flakes from a deaerated solution kept in a sealed container for 2 days. d) Digital photographs of  $d\text{-V}_2\text{CT}_x$  films indicating oxidation and color change in ambient atmosphere after a week and disintegration after a month (change in color from a grayish brown to black). e) High-resolution V 2p XPS spectrum of a fresh  $d\text{-V}_2\text{CT}_x$  film. f) High-resolution V 2p XPS spectrum of a  $d\text{-V}_2\text{CT}_x$  film after one month. g) XRD patterns of fresh and one-month old  $d\text{-V}_2\text{CT}_x$  films showing a significant reduction in the intensity and broadening of the characteristic (0002) peak of MXene. h) CVs of a fresh  $d\text{-V}_2\text{CT}_x$  film fabricated by vacuum filtration in 5 M LiCl at scan rates ranging from 2 to 100  $\text{mV s}^{-1}$ . i) Cyclic performance of a  $d\text{-V}_2\text{CT}_x$  film in 5 M LiCl at 20  $\text{mV s}^{-1}$ .

As schematically illustrated in **Figure 2a**, upon addition of concentrated alkali chloride solutions to dispersions of  $d\text{-V}_2\text{CT}_x$  flakes in water, electrostatic attractions between metal cations and the negatively charged MXene flakes lead to the assembly of multilayer restacked  $\text{V}_2\text{CT}_x$  flakes pillared by metal cations. **Figure 2b,c** compares the scanning electron microscopy (SEM) images of  $d\text{-V}_2\text{CT}_x$  flakes drop-casted onto alumina membranes before and after assembly using a concentrated solution of LiCl. In contrast to the  $d\text{-V}_2\text{CT}_x$  flakes, which were transparent to the electron beam (**Figure 2b**), the  $\text{V}_2\text{CT}_x$  flakes assembled by  $\text{Li}^+$  cations ( $\text{Li-V}_2\text{CT}_x$ ) appear to be much thicker and opaque (**Figure 2c**). AFM images of the  $\text{Li-V}_2\text{CT}_x$  flakes (**Figure S3c**, Supporting Information) show that they consist of several restacked MXene layers. High resolution scanning transmission electron microscopy (HR-STEM) images (shown in **Figure S5** of the Supporting Information) of these multilayered  $\text{V}_2\text{CT}_x$  flakes, assembled using either  $\text{Li}^+$  or  $\text{Na}^+$  cations ( $\text{Li-V}_2\text{CT}_x$  and  $\text{Na-V}_2\text{CT}_x$ ), showed that the stacking number of the flakes ranges between 8–10 and 10–13, respectively. The presence of alkali metals in the assembled  $\text{C-V}_2\text{CT}_x$  flakes (where C is Li, Na, or Mg) was confirmed by energy dispersive X-ray spectroscopy (EDS) and, for the case of Li, by X-ray photoelectron

spectroscopy (XPS) and inductively coupled plasma mass spectroscopy (ICP-MS), as shown in **Figure S6** and **Table S2** in the Supporting Information.

Freestanding films of assembled  $\text{C-V}_2\text{CT}_x$  flakes were fabricated by vacuum filtration of the relevant uniform dispersions in water (see the Experimental Section for details). **Figure 2d** shows a cross-sectional SEM image of a  $\text{Li-V}_2\text{CT}_x$  film where ordered stacking of MXene flakes resulted in a layered structure. The XRD analysis of the  $\text{C-V}_2\text{CT}_x$  films showed the characteristic MXene peaks for all samples (**Figure 2e** and **Figure S2c**, Supporting Information). The change in the position of the peak associated with the (0002) plane of the MXene is due to the dependence of the interlayer spacing on the type of cation present between the layers. Interestingly, the appearance of (0004), (0006), and (0008) MXene peaks in the XRD patterns of the assembled flakes suggest a more ordered structure for all  $\text{C-V}_2\text{CT}_x$  films compared to the one prepared using  $d\text{-V}_2\text{CT}_x$  (**Figure 1g**).<sup>[27,32]</sup> For  $\text{Li-V}_2\text{CT}_x$  films, the (0002) peak shifted from  $5.93^\circ$  for  $d\text{-V}_2\text{CT}_x$  to  $7.26^\circ$ . This corresponds to a decrease in the  $d$ -spacing of about 2.73 Å, which is probably caused by the attraction of the MXene layers to the interlayer  $\text{Li}^+$  cations. A similar decrease in the  $d$ -spacing has been previously

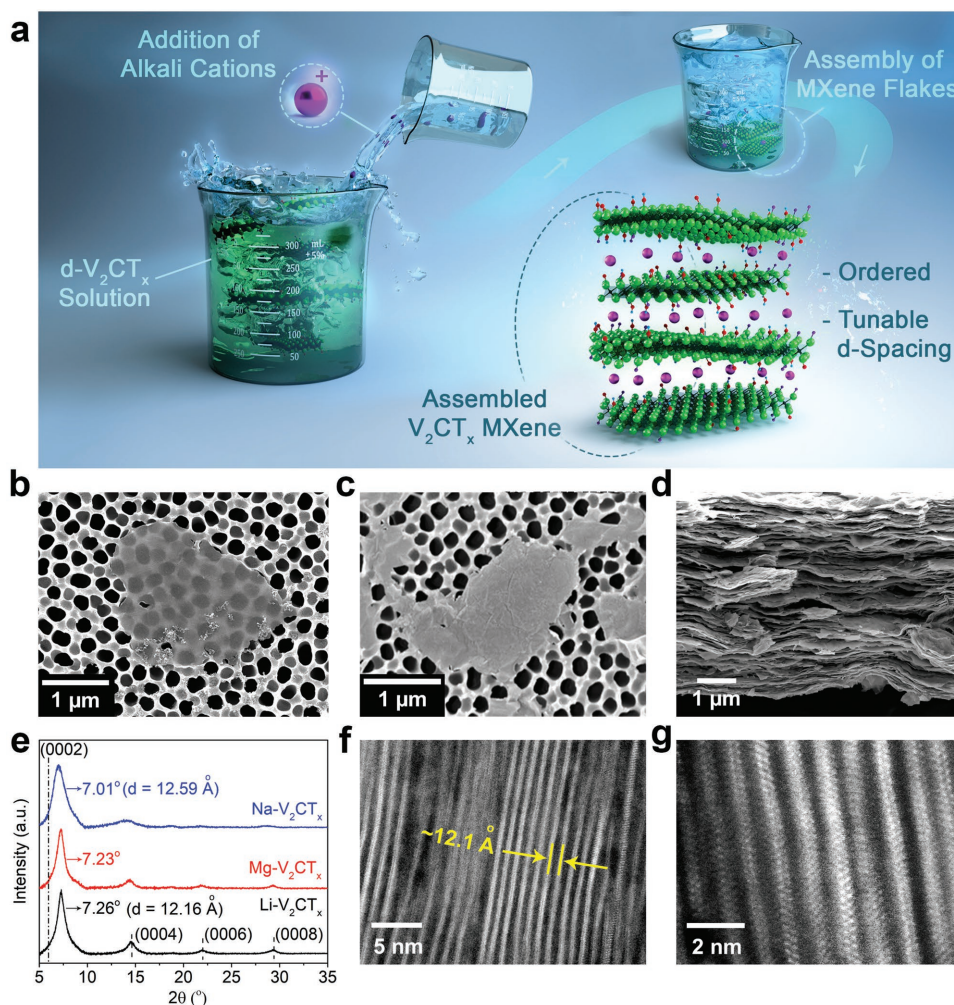


**Figure 2.** a) Schematic illustration of the cation-driven assembly process used for fabrication of the ordered and highly stable  $V_2CT_x$  flakes. b) SEM image of a freshly synthesized single-layer  $d-V_2CT_x$  on an alumina oxide (AAO) substrate. c) SEM image of  $V_2CT_x$  flakes restacked using  $Li^+$  cations ( $Li-V_2CT_x$ ) on an AAO filter. d) Cross-sectional SEM image of a  $Li-V_2CT_x$  film. e) XRD patterns of films fabricated using flakes assembled with various cations. The dashed line on the left of the graph indicates original position of the (0002) peak for  $d-V_2CT_x$  film. f) TEM image of a  $Li-V_2CT_x$  film showing its layered structure. g) Atomic resolution STEM image of the  $Na-V_2CT_x$ .

observed for layered  $Ti_3C_2T_x$  after electrochemical intercalation of  $Li^+$  into its structure.<sup>[33,34]</sup> Nevertheless, the assembled MXene films still showed quite high interlayer spacings, which suggests that the cations intercalated during assembly are in a (partially) hydrated state in the structure of the assembled  $V_2CT_x$  films.<sup>[35,36]</sup> Among the  $C-V_2CT_x$  films,  $Na-V_2CT_x$  showed the highest  $d$ -spacing of about 12.59 Å. Figure 2f,g displays HR-STEM images of the fabricated  $Li-V_2CT_x$  and  $Na-V_2CT_x$  films, showing the ordered layered structure of the films and confirming the  $d$ -spacing calculated from XRD.

In contrast to  $d-V_2CT_x$  films, the  $C-V_2CT_x$  films were very flexible (Figures S2 and S19, Supporting Information) and showed superior chemical stability in the ambient conditions. The XRD patterns of both  $Li-V_2CT_x$  and  $Na-V_2CT_x$  films after one month of storage under ambient atmosphere (Figure 3a) showed no change compared to the patterns of the as-fabricated films (shown in Figure 2e). Figure 3b shows the V 2p XPS spectrum of a fresh  $Li-V_2CT_x$  film. It is interesting to note that in this film, vanadium is present in more reduced forms compared to

$d-V_2CT_x$  films (Figure 1e). Deconvolution of the XPS spectra of  $Li-V_2CT_x$  before and after argon etching shows that  $V^{2+}$  and  $V^{3+}$  species are dominant in this sample ( $\approx 60$ – $68\%$ ). As shown in Figure 3c, in contrast to  $d-V_2CT_x$ ,  $V^{5+}$  species were not detected in the XPS analysis of  $Li-V_2CT_x$  even after one month of storage in air. Also, as shown in Figure 3d for  $Li-V_2CT_x$ , a freshly fabricated film is visually similar to those exposed to air at room temperature for one week and one month.

The combined evidence from a visual inspection of the films, the XRD data, and the XPS data imply that cation-driven assembly significantly suppresses the oxidation of the  $V_2CT_x$  flakes. We suggest that the suppression of oxidation is related to the charge transfer from the inserted alkali ions to the MXene flakes. The charge density difference that occurs after Li insertion into the interlayer space of  $V_2CT_2$  MXene with mixed  $-O$  and  $-F$  terminations, as calculated with density functional theory (DFT), is shown in Figure 3e. A significant reduction in charge density is found close to the Li atom. Bader charge analysis<sup>[37]</sup> revealed that each Li atom loses 0.8e, which

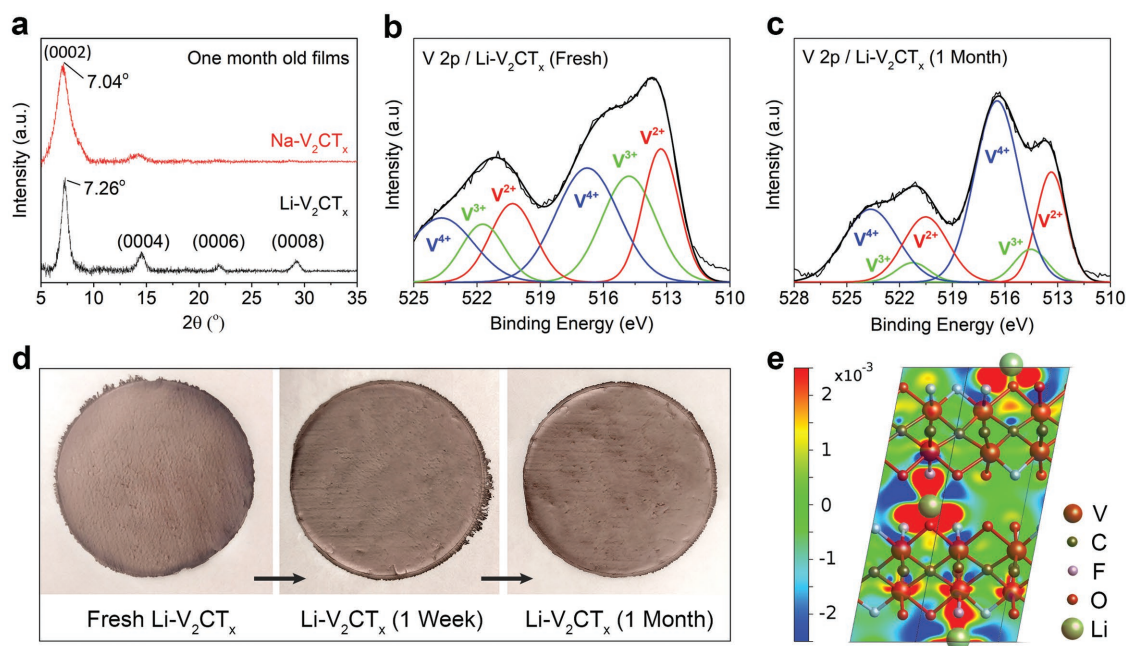


**Figure 3.** a) XRD patterns of the Li<sup>+</sup> and Na<sup>+</sup> assembled V<sub>2</sub>CT<sub>x</sub> films after one month of storage under ambient atmosphere. b) V 2p XPS spectrum of a fresh Li-V<sub>2</sub>CT<sub>x</sub> film. c) V 2p XPS spectrum of a Li-V<sub>2</sub>CT<sub>x</sub> after one month. d) Digital photographs of a Li-V<sub>2</sub>CT<sub>x</sub> film over time with no visual sign of degradation. e) Slices of charge density difference after lithiation, shown in a plane perpendicular to the MXene layer and through two intercalated Li atoms in the 3 × 3 unit cell. Here, red and blue colors indicate accumulation and depletion of charge density, respectively. The scale is in units of a u<sup>-3</sup>.

is transferred to the MXene layer. This charge is predominantly located on the terminating groups, particularly on the –F terminating atoms, which each gain approximately 0.2e while the –O terminating groups gain about 0.06e. On average, each V atom gains about 0.02e. This is in line with our XPS results that show the V species are in a more reduced state in Li-V<sub>2</sub>CT<sub>x</sub> compared to d-V<sub>2</sub>CT<sub>x</sub>. A similar charge transfer was previously calculated from sodium to V<sub>2</sub>CT<sub>2</sub>.<sup>[38]</sup>

The effects of cation-driven assembly on the electrochemical properties of MXenes was studied using Li-V<sub>2</sub>CT<sub>x</sub> and Na-V<sub>2</sub>CT<sub>x</sub> electrodes, which showed the smallest and largest interlayer spacing among the C-V<sub>2</sub>CT<sub>x</sub> films, respectively. **Figure 4a** compares the CV profiles of d-V<sub>2</sub>CT<sub>x</sub>, Li-V<sub>2</sub>CT<sub>x</sub>, and Na-V<sub>2</sub>CT<sub>x</sub> electrodes in a 5 m LiCl aqueous electrolyte. All CV curves show similar near-rectangular shapes with some broad redox peaks. The CV responses of the electrodes are typical of intercalation-based pseudocapacitive electrode materials, such as those previously reported for Ti<sub>3</sub>C<sub>2</sub>T<sub>x</sub> MXene.<sup>[12,34,39]</sup> In MXene electrodes the charge storage is accompanied by fast intercalation of ions allowing the redox reactions to occur in the bulk of the electrode and at the surface of individual MXene layers.<sup>[11]</sup> At the same scan rate of 2 mV s<sup>-1</sup>, the area under the CV curves and the specific capacitance of Li-V<sub>2</sub>CT<sub>x</sub> and Na-V<sub>2</sub>CT<sub>x</sub> electrodes are significantly larger than that of the d-V<sub>2</sub>CT<sub>x</sub> electrode. This can be explained by the pillaring effect of the cations between MXene layers and the more ordered structure of the assembled MXene electrodes which is expected to improve both ionic and electronic transport properties of the electrodes. As explained above, Na-V<sub>2</sub>CT<sub>x</sub> had a larger interlayer spacing compared to Li-V<sub>2</sub>CT<sub>x</sub> and, as a result, it showed better electrochemical properties, especially at higher scan rates (Figure 4c and Figure S8a,

Supporting Information). Nevertheless, the CV profiles of Li-V<sub>2</sub>CT<sub>x</sub> and Na-V<sub>2</sub>CT<sub>x</sub> were quite similar, offering a larger potential window (1 V) than previously reported MXene electrodes tested in aqueous electrolytes.<sup>[5]</sup> An important property of assembled C-V<sub>2</sub>CT<sub>x</sub> electrodes is that they can intercalate cations of different charges and sizes. CV profiles of Na-V<sub>2</sub>CT<sub>x</sub> in various sulfate electrolytes (containing Li<sup>+</sup>, Na<sup>+</sup>, K<sup>+</sup>, Mg<sup>2+</sup>, Zn<sup>2+</sup>, and Al<sup>3+</sup> cations) are shown in Figure 4b. Different CV shapes, as well as different capacitance values obtained in different electrolytes with similar anionic species, indicate that cation intercalation (and the associated redox reactions occurring at MXene surfaces upon their insertion) is the dominant charge storage mechanism in C-V<sub>2</sub>CT<sub>x</sub> electrodes.

Gravimetric capacitances of Na-V<sub>2</sub>CT<sub>x</sub> electrodes in different electrolytes are shown in Figure 4c at scan rates ranging from 2 to 100 mV s<sup>-1</sup>. Depending on the electrolyte and intercalating cations, Na-V<sub>2</sub>CT<sub>x</sub> electrodes showed specific capacitances ranging from ≈120 to ≈285 F g<sup>-1</sup>. These capacitance values are around three times higher than reported values for freestanding films of d-Ti<sub>3</sub>C<sub>2</sub>T<sub>x</sub> in electrolytes containing similar cations.<sup>[5]</sup>

Figure 4d shows the cycle life performance of Na-V<sub>2</sub>CT<sub>x</sub> electrodes in different electrolytes at 10 A g<sup>-1</sup>. Regardless of the electrolyte used and intercalating cations, Na-V<sub>2</sub>CT<sub>x</sub> electrodes showed excellent cyclic performance with no capacity decay after 10 000 cycles and Coulombic efficiencies of about 100%, confirming the significantly improved stability of the assembled electrodes compared to d-V<sub>2</sub>CT<sub>x</sub> electrodes. It is interesting to note that for electrolytes with larger cations, such as MgSO<sub>4</sub> and K<sub>2</sub>SO<sub>4</sub>, the specific capacitance of the electrodes initially increased before becoming constant. The CV profiles of Na-V<sub>2</sub>CT<sub>x</sub> in these electrolytes (Figure S9, Supporting Information)

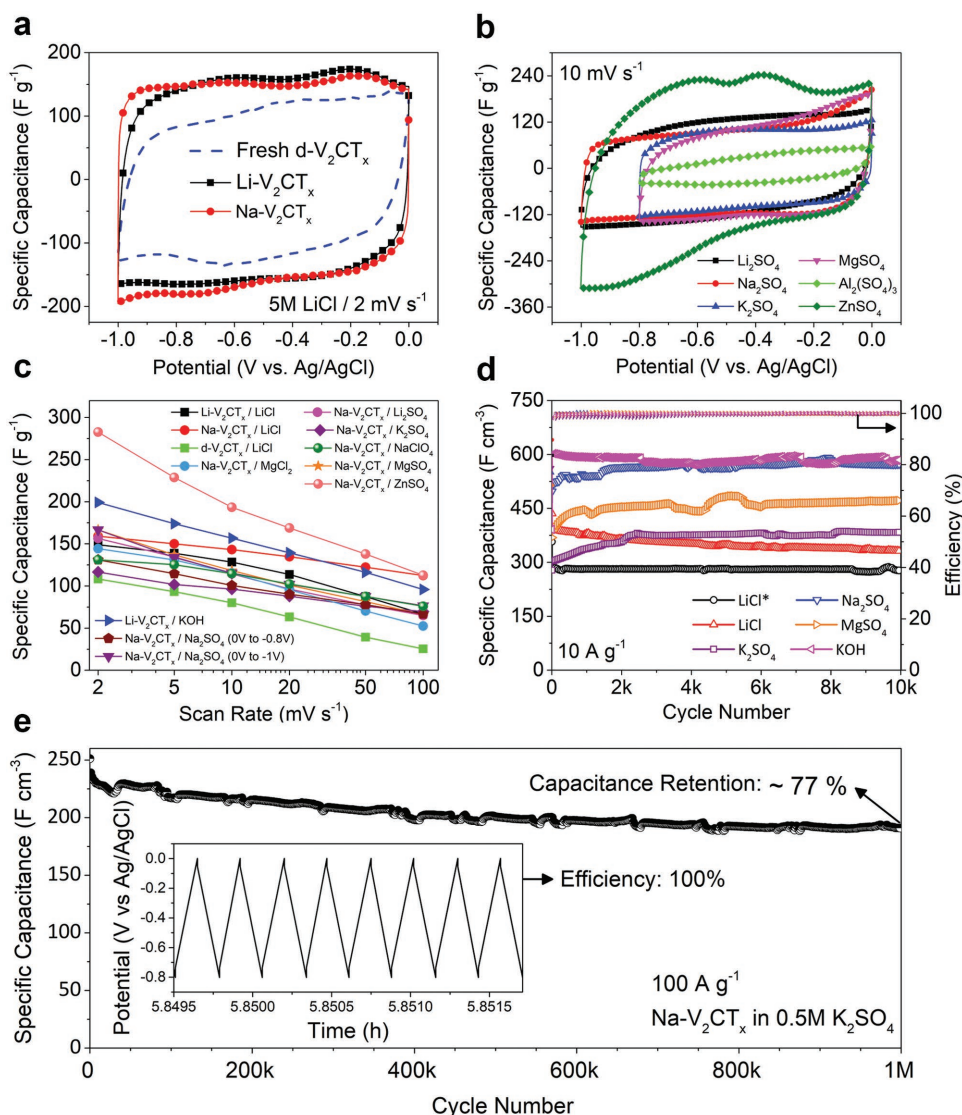


**Figure 4.** a) CV profiles of d-V<sub>2</sub>CT<sub>x</sub>, Li-V<sub>2</sub>CT<sub>x</sub>, and Na-V<sub>2</sub>CT<sub>x</sub> electrodes in 5 M LiCl electrolyte (scan rate = 2 mV s<sup>-1</sup>). b) CVs of Na-V<sub>2</sub>CT<sub>x</sub> in various electrolytes. c) Gravimetric capacitance of different V<sub>2</sub>CT<sub>x</sub> electrodes in various salt electrolytes. d) Cyclic performance of Na-V<sub>2</sub>CT<sub>x</sub> electrodes in various electrolytes at 10 A g<sup>-1</sup>. (\*) indicates working electrode was Li-V<sub>2</sub>CT<sub>x</sub>. e) Cycle life performance of an Na-V<sub>2</sub>CT<sub>x</sub> electrode in a K<sub>2</sub>SO<sub>4</sub> electrolyte with an efficiency of 100% and ≈77% capacitance retention after one million cycles at a rate of 100 A g<sup>-1</sup>.

showed a gradual increase in current during cycling. This can be explained by an initial slow diffusion or intercalation rate of the larger cations into the electrode, which improves during successive charge/discharge cycles. A similar behavior was reported for d-Ti<sub>3</sub>C<sub>2</sub>T<sub>x</sub> in a MgSO<sub>4</sub> electrolyte, where maximum capacity was achieved after 48 h of continued cycling.<sup>[5]</sup>

To investigate the limits of rate handling and cyclic life of the assembled MXene electrodes, a Na-V<sub>2</sub>CT<sub>x</sub> electrode was subjected to galvanostatic charge/discharge (GCD) cycling in a K<sub>2</sub>SO<sub>4</sub> electrolyte at a current density of 100 A g<sup>-1</sup> (Figure 4e). At this high current rate, the Na-V<sub>2</sub>CT<sub>x</sub> electrode showed a volumetric capacity of ≈250 F cm<sup>-3</sup> with capacitance retention of ≈77% after one million cycles. To the best of our knowledge, no other pseudocapacitive material has been reported to date with such excellent cyclic performance and lifetime. Furthermore, CV profiles of Na-V<sub>2</sub>CT<sub>x</sub> (shown in Figure S10, Supporting

Information) remained almost rectangular at scan rates of up to 1000 mV s<sup>-1</sup>, indicating their high-rate handling capability.<sup>[5]</sup>

Clearly, the electrochemical performance of Na-V<sub>2</sub>CT<sub>x</sub> electrodes in electrolytes containing various inorganic cations surpasses the reported performance of d-Ti<sub>3</sub>C<sub>2</sub>T<sub>x</sub> films. However, previous studies have shown that Ti<sub>3</sub>C<sub>2</sub>T<sub>x</sub> achieves its highest capacitance in H<sub>2</sub>SO<sub>4</sub> electrolytes.<sup>[3,13,25,40–42]</sup> This high capacitance is due to the change in the oxidation state of Ti accompanied by the protonation of oxygen surface groups during redox reactions in the H<sub>2</sub>SO<sub>4</sub> electrolytes.<sup>[43]</sup> As a result of the redox reactions, the CV curves of Ti<sub>3</sub>C<sub>2</sub>T<sub>x</sub> in H<sub>2</sub>SO<sub>4</sub> electrolytes show distinct reversible redox peaks.<sup>[3,13]</sup> In order to make a direct comparison, we investigated the capacitive performance of Na-V<sub>2</sub>CT<sub>x</sub> electrodes in a 3 M H<sub>2</sub>SO<sub>4</sub> electrolyte. CV tests of the electrodes (Figure 5a) showed a pair of broad and highly reversible redox peaks at ≈0 V (vs Ag/AgCl). The electrodes showed

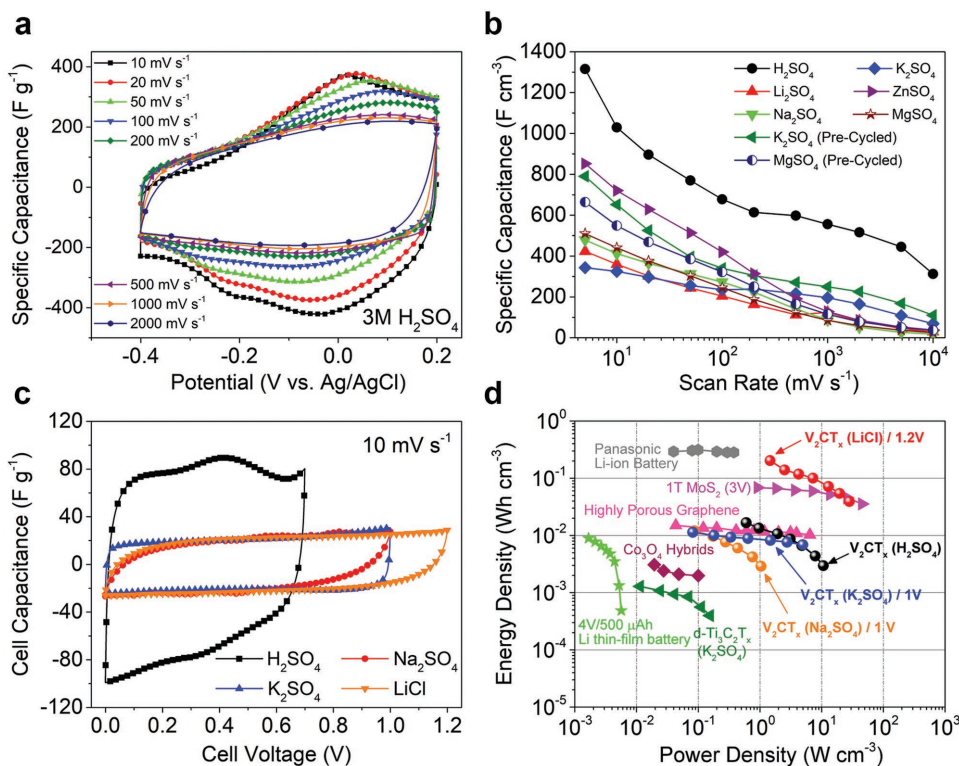


**Figure 5.** a) CV profiles of a Na-V<sub>2</sub>CT<sub>x</sub> electrode in a 3 M H<sub>2</sub>SO<sub>4</sub> electrolyte at scan rates from 10 mV s<sup>-1</sup> to 2 V s<sup>-1</sup>. b) Capacitance and rate performance of 3–4 μm thick Na-V<sub>2</sub>CT<sub>x</sub> electrodes in various sulfate-based electrolytes. c) CV profiles of symmetric supercapacitors assembled using Na-V<sub>2</sub>CT<sub>x</sub> electrodes in various electrolytes. d) Ragone plot of Na-V<sub>2</sub>CT<sub>x</sub> symmetric supercapacitors comparing the energy (*E*) and power (*P*) density of symmetric Na-V<sub>2</sub>CT<sub>x</sub> cells to other supercapacitor and battery systems reported in the literature: Ti<sub>3</sub>C<sub>2</sub>T<sub>x</sub> MXene,<sup>[5]</sup> Panasonic Li-ion batteries,<sup>[5,40]</sup> 1T MoS<sub>2</sub>,<sup>[40]</sup> Co<sub>3</sub>O<sub>4</sub>/Co(OH)<sub>2</sub> hybrids,<sup>[45]</sup> highly porous graphene,<sup>[40]</sup> and Li-thin-film battery.<sup>[5]</sup> The *E* and *P* values were calculated based on the total volume of the MXene electrodes.

a highly capacitive response up to a very high scan rate of 2 V s<sup>-1</sup>. The highest specific capacitances of ≈1315 F cm<sup>-3</sup> and ≈420 F g<sup>-1</sup>, were found at a scan rate of 5 mV s<sup>-1</sup>. These volumetric and gravimetric capacitances are on average higher by ≈400 F cm<sup>-3</sup> and ≈150 F g<sup>-1</sup>, respectively, than the capacitance of freestanding Ti<sub>3</sub>C<sub>2</sub>T<sub>x</sub> film electrodes with comparable thicknesses<sup>[13]</sup> and about two times higher than the specific capacitance of 1T MoS<sub>2</sub> electrodes.<sup>[44]</sup> For Ti<sub>3</sub>C<sub>2</sub>T<sub>x</sub>, similar high-rate pseudocapacitive response has been observed only for structurally engineered hydrogel and porous electrodes.<sup>[3]</sup> GCD tests (Figure S12d, Supporting Information) showed that the drop in the specific capacitance of the electrodes with increasing the current density is relatively small. At a very high current density of 100 A g<sup>-1</sup>, the Na-V<sub>2</sub>CT<sub>x</sub> electrode showed an outstanding capacitance of ≈200 F g<sup>-1</sup> (volumetric capacitance of 600 F cm<sup>-3</sup>).

The volumetric capacitance and rate capability of Na-V<sub>2</sub>CT<sub>x</sub> electrodes in electrolytes comprised of sulfate anions and various cations are compared in Figure 5b. While the highest specific capacitance at each scan rate was achieved in an H<sub>2</sub>SO<sub>4</sub> electrolyte, the performance of the electrodes were very impressive in all other studied electrolytes. For example, at a scan rate of 5 mV s<sup>-1</sup> volumetric capacitances of ≈852, ≈790, and ≈664 F cm<sup>-3</sup> were achieved in ZnSO<sub>4</sub>, K<sub>2</sub>SO<sub>4</sub>, and MgSO<sub>4</sub> electrolytes, respectively. The excellent capacitive performance and ion transport properties of Na-V<sub>2</sub>CT<sub>x</sub> electrodes in various

electrolytes were also confirmed by electrochemical impedance spectroscopy (EIS) measurements (Figure S13, Supporting Information).

To investigate the performance of C-V<sub>2</sub>CT<sub>x</sub> electrodes in supercapacitor devices, we fabricated symmetric cells using these electrodes and tested their performance in various electrolytes. Figure 5c shows the CV curves of Na-V<sub>2</sub>CT<sub>x</sub> symmetric supercapacitors in H<sub>2</sub>SO<sub>4</sub>, Na<sub>2</sub>SO<sub>4</sub>, K<sub>2</sub>SO<sub>4</sub>, and LiCl electrolytes at a scan rate of 10 mV s<sup>-1</sup>.

The largest potential window of 1.2 V was obtained when a LiCl solution was used as the electrolyte. However, as expected, when an H<sub>2</sub>SO<sub>4</sub> solution was used as the electrolyte, the highest output current and specific capacitance was achieved. Figure 5d shows a Ragone plot comparing the volumetric performance of the Na-V<sub>2</sub>CT<sub>x</sub> symmetric supercapacitors with some of the other notable symmetric supercapacitors and batteries reported in the literature. It should be noted that the volumetric power and energy densities of Na-V<sub>2</sub>CT<sub>x</sub> symmetric cells in some electrolytes, such as K<sub>2</sub>SO<sub>4</sub>, are an order of magnitude higher than those reported for symmetric d-Ti<sub>3</sub>C<sub>2</sub>T<sub>x</sub> cells in the same electrolytes.<sup>[5]</sup> Moreover, Na-V<sub>2</sub>CT<sub>x</sub> symmetric cells in LiCl electrolyte showed a power density of 1.46 W cm<sup>-3</sup> at an energy density of 0.2 Wh cm<sup>-3</sup>. The energy density of the cell reached 0.04 Wh cm<sup>-3</sup> at a high power density of 28.15 W cm<sup>-3</sup>. These promising results place the V<sub>2</sub>CT<sub>x</sub> MXene among the best pseudocapacitive materials reported to date.<sup>[5,13,44,46–48]</sup>

The application of cation-driven assembly to fabricate high performance and stable electrodes from unstable MXene flakes is not limited to  $V_2CT_x$ . As shown in Figure S14 of the Supporting Information, we also applied the same assembly and electrode fabrication methods to delaminated  $Ti_2CT_x$  MXene (which, similar to  $V_2CT_x$ , is very unstable after delamination) and were able to fabricate freestanding C- $Ti_2CT_x$  films with capacitances of  $\approx 172\text{ F g}^{-1}$  and  $\approx 640\text{ F cm}^{-3}$  at  $2\text{ mV s}^{-1}$  in a LiCl electrolyte, with no loss of capacity in over 10 000 cycles.

In summary, we have demonstrated a cation-driven assembly process to fabricate highly stable pseudocapacitive electrodes with superior electrochemical properties from otherwise unstable 2D  $V_2CT_x$  MXene flakes. Electrochemical tests in neutral electrolytes with various inorganic cations showed that the electrodes can be intercalated with cations of various sizes and charges. In an  $H_2SO_4$  electrolyte, electrodes fabricated using the assembled  $V_2CT_x$  flakes showed outstanding specific capacitances, reaching values as high as  $\approx 420\text{ F g}^{-1}$  and  $\approx 1315\text{ F cm}^{-3}$ , surpassing the performance of many state-of-the-art supercapacitor materials.<sup>[5,13,44,46,47]</sup> The C- $V_2CT_x$  electrodes show excellent high-rate capability and deliver specific capacitances of  $\approx 180$  and  $\approx 100\text{ F g}^{-1}$  at high scan rates of 1 and  $10\text{ V s}^{-1}$ , respectively, higher than the measured specific capacitances of d- $Ti_3C_2T_x$  film electrodes at these scan rates.<sup>[13]</sup> We also demonstrated the impact of cation-driven assembly on the electrochemical stability and cyclic performance of  $V_2CT_x$ . The fabricated electrodes showed no capacitance decay after 10 000 cycles at  $10\text{ A g}^{-1}$  and a capacitance retention of  $\approx 77\%$  after one million cycles at a rate of  $100\text{ A g}^{-1}$ , showcasing a new standard for pseudocapacitive materials with ultralong cycle life. This study reveals high-performance and stable pseudocapacitive behavior of 2D MXenes beyond  $Ti_3C_2T_x$ . Considering that more than 20 different MXene compositions are synthesized so far, and many more predicted to exist, this study paves the way to designing next-generation pseudocapacitive materials for ECs based on MXenes.

## Supporting Information

Supporting Information is available from the Wiley Online Library or from the author.

## Acknowledgements

The authors thank W. Liang for help with TEM analysis. This work was supported by the startup funds and intramural grants program (IGP) at Auburn University, as well as by the National Science Foundation (EFMA-1542707). XRD and SEM analysis were carried out at the Department of Materials Engineering at Auburn University. XPS analyses were performed at the Central Analytical facility at the University of Alabama. TEM imaging was performed at Northeastern University's Kostas Advanced Nanocharacterization Facility (KANCF), Burlington, MA. The authors thank H. Chen for help with materials preparation. A.V.M. was supported by Alabama EPSCoR Graduate Research Scholar Program (GRSP Round 12 and 13) doctoral fellowship.

## Conflict of Interest

The authors declare no conflict of interest.

## Keywords

2D vanadium carbide, assembly, MXenes, pseudocapacitance, supercapacitors

Received: October 26, 2018

Revised: November 17, 2018

Published online: December 27, 2018

- [1] V. Augustyn, P. Simon, B. Dunn, *Energy Environ. Sci.* **2014**, *7*, 1597.
- [2] P. Simon, Y. Gogotsi, *Nat. Mater.* **2008**, *7*, 845.
- [3] M. R. Lukatskaya, S. Kota, Z. Lin, M. Q. Zhao, N. Shpigel, M. D. Levi, J. Halim, P. L. Taberna, M. W. Barsoum, P. Simon, Y. Gogotsi, *Nat. Energy* **2017**, *6*, 1.
- [4] X. Yu, S. Yun, J. S. Yeon, P. Bhattacharya, L. Wang, S. W. Lee, X. Hu, H. S. Park, *Adv. Energy Mater.* **2018**, *8*, 1.
- [5] M. R. Lukatskaya, O. Mashtalir, C. E. Ren, Y. Dall'Agnese, P. Rozier, P. L. Taberna, M. Naguib, P. Simon, M. W. Barsoum, Y. Gogotsi, *Science* **2013**, *341*, 1502.
- [6] M. Beidaghi, Y. Gogotsi, *Energy Environ. Sci.* **2014**, *7*, 867.
- [7] M. R. Lukatskaya, B. Dunn, Y. Gogotsi, *Nat. Commun.* **2016**, *7*, 1.
- [8] D. Choi, G. E. Blomgren, P. N. Kumta, *Adv. Mater.* **2006**, *18*, 1178.
- [9] J. P. Zheng, P. J. J. Cygan, T. R. R. Jow, *J. Electrochem. Soc.* **1995**, *142*, 2699.
- [10] P. Geng, S. Zheng, H. Tang, R. Zhu, L. Zhang, S. Cao, H. Xue, H. Pang, *Adv. Energy Mater.* **2018**, *8*, 1703259.
- [11] V. Augustyn, J. Come, M. A. Lowe, J. W. Kim, P.-L. Taberna, S. H. Tolbert, H. D. Abruña, P. Simon, B. Dunn, *Nat. Mater.* **2013**, *12*, 518.
- [12] M. Okubo, A. Sugahara, S. Kajiyama, A. Yamada, *Acc. Chem. Res.* **2018**, *51*, 591.
- [13] M. Ghidui, M. R. Lukatskaya, M. Q. Zhao, Y. Gogotsi, M. W. Barsoum, *Nature* **2015**, *516*, 78.
- [14] M. Naguib, O. Mashtalir, J. Carle, V. Presser, J. Lu, L. Hultman, Y. Gogotsi, M. W. Barsoum, *ACS Nano* **2012**, *6*, 1322.
- [15] M. Naguib, V. N. Mochalin, M. W. Barsoum, Y. Gogotsi, *Adv. Mater.* **2014**, *26*, 992.
- [16] M. Alhabeab, K. Maleski, T. S. Mathis, A. Sarycheva, C. B. Hatter, S. Uzun, A. Levitt, Y. Gogotsi, *Angew. Chem.* **2018**, *130*, 5542.
- [17] B. Anasori, M. R. Lukatskaya, Y. Gogotsi, *Nat. Rev. Mater.* **2017**, *2*, 16098.
- [18] M. Naguib, R. R. Unocic, B. L. Armstrong, J. Nanda, *Dalton Trans.* **2015**, *44*, 9353.
- [19] A. VahidMohammadi, A. Hadjikhani, S. Shahbazmohamadi, M. Beidaghi, *ACS Nano* **2017**, *11*, 11135.
- [20] M. Naguib, J. Halim, J. Lu, K. M. Cook, L. Hultman, Y. Gogotsi, M. W. Barsoum, *J. Am. Chem. Soc.* **2013**, *135*, 15966.
- [21] Q. Shan, X. Mu, M. Alhabeab, C. E. Shuck, D. Pang, X. Zhao, X.-F. Chu, Y. Wei, F. Du, G. Chen, Y. Gogotsi, Y. Gao, Y. Dall'Agnese, *Electrochem. Commun.* **2018**, *96*, 103.
- [22] Y. Xie, Y. Dall'Agnese, M. Naguib, Y. Gogotsi, M. W. Barsoum, H. L. Zhuang, P. R. C. Kent, *ACS Nano* **2014**, *8*, 9606.
- [23] C. J. Zhang, S. Pinilla, N. McEvoy, C. P. Cullen, B. Anasori, E. Long, S. H. Park, A. Seral-Ascaso, A. Shmeliov, D. Krishnan, C. Morant, X. Liu, G. S. Duesberg, Y. Gogotsi, V. Nicolosi, *Chem. Mater.* **2017**, *29*, 4848.
- [24] R. Lotfi, M. Naguib, D. E. Yilmaz, J. Nanda, A. C. T. van Duin, *J. Mater. Chem. A* **2018**, *199*, 393.
- [25] Y. Xia, T. S. Mathis, M. Q. Zhao, B. Anasori, A. Dang, Z. Zhou, H. Cho, Y. Gogotsi, S. Yang, *Nature* **2018**, *557*, 409.
- [26] S. M. Bak, R. Qiao, W. Yang, S. Lee, X. Yu, B. Anasori, H. Lee, Y. Gogotsi, X. Q. Yang, *Adv. Energy Mater.* **2017**, *7*, 1700959.

- [27] J. Lim, X. Jin, Y. K. Jo, S. Lee, S. J. Hwang, *Angew. Chem., Int. Ed.* **2017**, *56*, 7093.
- [28] K. Lu, Z. Hu, Z. Xiang, J. Ma, B. Song, J. Zhang, H. Ma, *Angew. Chem., Int. Ed.* **2016**, *55*, 10448.
- [29] Q. Cheng, T. Yang, Y. Li, M. Li, C. K. Chan, *J. Mater. Chem. A* **2016**, *4*, 6902.
- [30] H. P. Shasha Zheng, H. Xue, *Coord. Chem. Rev.* **2018**, *373*, 2.
- [31] J. Heising, M. G. Kanatzidis, *J. Am. Chem. Soc.* **1999**, *121*, 11720.
- [32] D. Zhao, M. Clites, G. Ying, S. Kota, J. Wang, V. Natu, X. Wang, E. Pomerantseva, M. Cao, M. W. Barsoum, *Chem. Commun.* **2018**, *54*, 4533.
- [33] J. Come, J. M. Black, M. R. Lukatskaya, M. Naguib, M. Beidaghi, A. J. Rondinone, S. V. Kalinin, D. J. Wesolowski, Y. Gogotsi, N. Balke, *Nano Energy* **2015**, *17*, 27.
- [34] M. D. Levi, M. R. Lukatskaya, S. Sigalov, M. Beidaghi, N. Shpigel, L. Daikhin, D. Aurbach, M. W. Barsoum, Y. Gogotsi, *Adv. Energy Mater.* **2015**, *5*, 1400815.
- [35] M. Ghidui, J. Halim, S. Kota, D. Bish, Y. Gogotsi, M. W. Barsoum, *Chem. Mater.* **2016**, *28*, 3507.
- [36] N. C. Osti, M. Naguib, A. Ostadhossein, Y. Xie, P. R. C. Kent, B. Dyatkin, G. Rother, W. T. Heller, A. C. T. van Duin, Y. Gogotsi, E. Mamontov, *ACS Appl. Mater. Interfaces* **2016**, *8*, 8859.
- [37] G. Henkelman, A. Arnaldsson, H. Jónsson, *Comput. Mater. Sci.* **2006**, *36*, 354.
- [38] N. M. Caffrey, *Nanoscale* **2018**, *10*, 13520.
- [39] Y. Gogotsi, R. M. Penner, *ACS Nano* **2018**, *12*, 2081.
- [40] M. Boota, B. Anasori, C. Voigt, M. Q. Zhao, M. W. Barsoum, Y. Gogotsi, *Adv. Mater.* **2016**, *28*, 1517.
- [41] A. VahidMohammadi, J. Moncada, H. Chen, E. Kayali, J. Orangi, C. A. Carrero, M. Beidaghi, *J. Mater. Chem. A* **2018**, *6*, 22123.
- [42] J. Yan, C. E. Ren, K. Maleski, C. B. Hatter, B. Anasori, P. Urbankowski, A. Sarycheva, Y. Gogotsi, *Adv. Funct. Mater.* **2017**, *27*, 1701264.
- [43] M. R. Lukatskaya, S. M. Bak, X. Yu, X. Q. Yang, M. W. Barsoum, Y. Gogotsi, *Adv. Energy Mater.* **2015**, *5*, 1500589.
- [44] M. Acerce, D. Voiry, M. Chhowalla, *Nat. Nanotechnol.* **2015**, *10*, 313.
- [45] H. Pang, X. Li, Q. Zhao, H. Xue, W. Y. Lai, Z. Hu, W. Huang, *Nano Energy* **2017**, *35*, 138.
- [46] M. F. El-Kady, M. Ihns, M. Li, J. Y. Hwang, M. F. Mousavi, L. Chaney, A. T. Lech, R. B. Kaner, *Proc. Natl. Acad. Sci. USA* **2015**, *112*, 4233.
- [47] Z. Wen, X. Wang, S. Mao, Z. Bo, H. Kim, S. Cui, G. Lu, X. Feng, J. Chen, *Adv. Mater.* **2012**, *24*, 5610.
- [48] L. Wang, X. Feng, L. Ren, Q. Piao, J. Zhong, Y. Wang, H. Li, Y. Chen, B. Wang, *J. Am. Chem. Soc.* **2015**, *137*, 4920.